SPECTRAL ANALYSIS OF ENERGY TRANSPORT PROCESSES IN TURBULENT FLOW OVER CIRCULAR-ARC RIBS

Wei-Jian Xiong, Jinglei Xu
State Key Laboratory of Mechanics and Control of Aeronautics and Astronautics Structures
Nanjing University of Aeronautics and Astronautics
29th Yudao Street, Nanjing, China
xwj@nuaa.edu.cn, xujl@nuaa.edu.cn

Bing-Chen Wang
Department of Mechanical Engineering, University of Manitoba,
Winnipeg, MB, R3T 5V6, Canada
BingChen.Wang@Umanitoba.Ca

ABSTRACT

Energy transport processes in turbulent flow through a channel roughened by circular-arc ribs of different pitch-to-height ratios ($P/H = 3.0$, 5.0 and 7.5) at a fixed Reynolds number of $Re_b = 5600$ are studied in the spectral space using direct numerical simulations (DNS). The characteristic spanwise wavelengths of turbulent motions are investigated through a spectral analysis of the transport equation of turbulence kinetic energy (TKE). It is observed that the turbulent production term is approximately balanced by the interscale transport and dissipation terms associated with small-scale turbulent motions in the inter-rib regions. It is also interesting to observe that as the value of P/H increases, the TKE production for sustaining large-scale motions strengthens gradually, whereas the backscatter of TKE from medium- to large-scale turbulence structures becomes increasingly suppressed.

INTRODUCTION

Circular-arc ribs are frequently used for enhancing turbulent transport of momentum and thermal energy for turbine blade cooling and heat exchangers (Prasad & Saini, 1988). In this class of flows, large flow separation region arises from continuous arc surfaces, and the flow separation positions are sensitive to the pitch-to-height ratio. Turbulent motions are inhomogeneous along the streamwise and vertical directions, featuring coherent vortices with various spatial and temporal scales. These physical features greatly complicate the energy transport processes associated with turbulent motions of different scales, making the characteristic scales of the turbulence structures fundamentally different from those of a 2-D smooth-wall plane-channel flow (Hoyas & Jiménez, 2006).

The transport equations of Reynolds stresses are useful for investigating turbulence energy balance in turbulent flows. Following the fundamental work of Mansour *et al.* (1988), turbulent transport of Reynolds stresses has been studied extensively in the physical space using DNS in the contexts of turbulent channel flows, Couette flows and boundary-layer flows. Since the seminal work of Lumley (1964), DNS study of transport of Reynolds stresses has been extended from the physical space to the spectral space, which is useful for precisely identifying the characteristic wavelengths of turbulence structures. The number of studies on spectral analyses of turbulent energy transport processes is still very limited in the current literature, focusing almost exclusively on DNS of smooth-wall channel flows (Mizuno, 2016; Yang *et al.*, 2020). Thus far, no high-fidelity DNS study on transport of turbulent stresses and TKE in the spectral space has been reported in the context of a rib roughened boundary-layer flow.

In view of this knowledge gap, we aim at performing a detailed DNS study of turbulent channel flows with circular-arc ribs mounted on one wall to investigate the pitch-to-height ratio effects on the transport processes of TKE in the spectral space. The characteristic wavelengths of turbulent motions responsible for the TKE transport among budget terms such as convection, production, diffusion, pressure-strain and dissipation are studied, and the mechanisms of interscale transport are also investigated.

TEST CASES AND NUMERICAL ALGORITHM

Figure 1 shows the schematic of the computational domain and coordinate system. Here x, y and z denote the streamwise, wall-normal and spanwise coordinates, and u, v and w represent the three corresponding velocity components, respectively. The streamwise length is set to $L_x = 12\delta$, where δ is the half channel height. In the spanwise direction, the domain length is set to $L_z = 2\pi\delta$. The pitch and height of the circular-arc ribs are P and H, respectively. For all three ribbed channel flow cases considered, the radius of the arc is kept constant, i.e. $R = 0.2\delta$. Cases P1, P2 and P3 are compared to investigate the effects of the pitch-to-height ratio (for $P/H = 3.0$, 5.0 and 7.5, respectively) on the flow field based on a common blockage ratio (i.e., $Br = H/2\delta = 0.1$). Due to the fixed domain size, cases P1, P2 and P3 consist of 20, 12 and 8 periods, respectively. The Reynolds number is fixed at $Re_b = 2\delta U_b/\nu = 5600$ to maintain a constant mass flow rate, where U_b denotes the bulk mean velocity. In order to identify the rib effects, an additional case of a smooth channel flow (denoted as case SC) at $Re_b = 5600$ that follows Kim et al. (1987) has been simulated for the purpose of comparison. The flow field is fully developed and periodic boundary conditions are applied to both streamwise and spanwise directions. A no-slip boundary condition is imposed on all solid surfaces.

The DNS is performed using a spectral-element code so-called "Semtex" contributed by Blackburn & Sherwin (2004). This code is developed using C++ and FORTRAN programming languages, and parallelized using message passing interface (MPI) libraries. All physical quantities were expanded into the spectral space using Fourier series in the spanwise (z) direction, and 240 Fourier modes were used in each test case with a grid resolution of $5.3 \leq \Delta_z^+ \leq 5.9$ (measured in wall unit based on $u_{\tau S}$, the average friction velocity over the top smooth wall). Quadrilateral spectral-elements were used

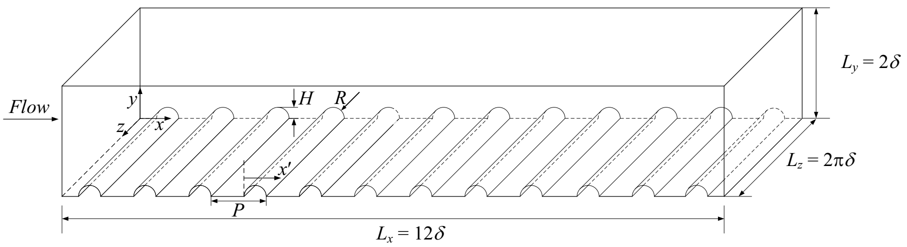

Figure 1. Schematic diagram of the computational domain and the coordinate systems. The origin of the absolute coordinate system $[x, y, z]$ is located at the inner bottom corner of the inlet and the origin of the relative streamwise coordinate x' is located at the windward face of each rib, which is defined to facilitate the analysis of the repeated rib period.

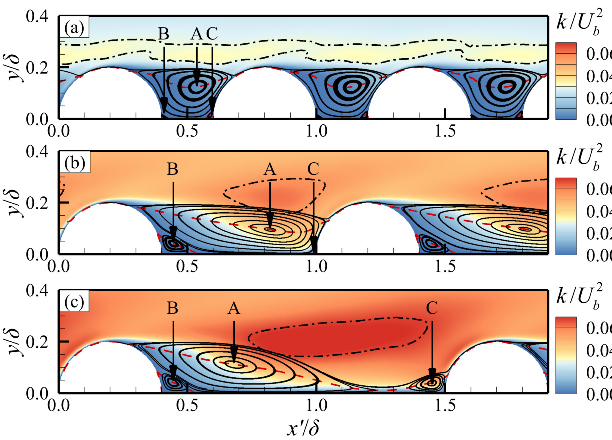

Figure 2. Mean streamlines with contours of non-dimensional turbulence kinetic energy k/U_b^2 for all four ribbed cases. Panels (a)-(c) correspond to cases P1, P2 and P3, respectively. The dot-dashed line demarcates the isopleth of $k = 0.9\max(k)$ for each cases. The red dashed line demarcates the isopleth of $\langle u \rangle = 0$.

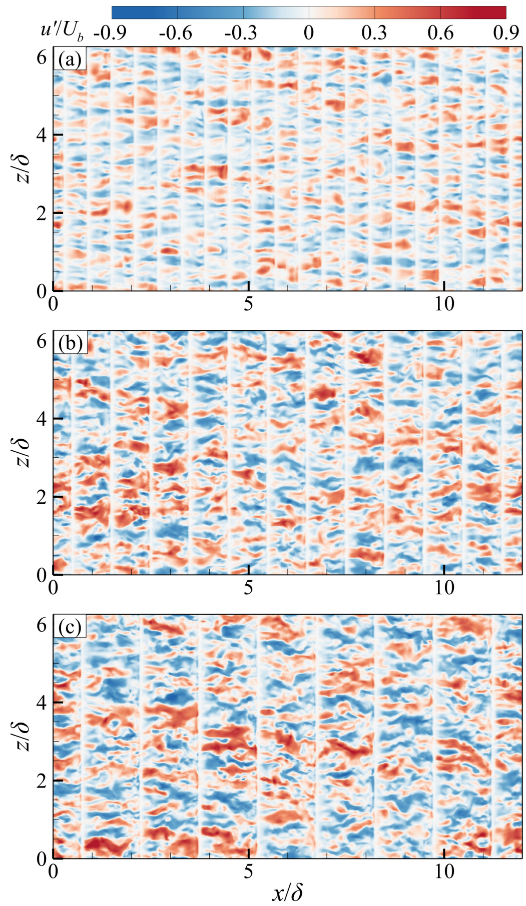

Figure 3. Contours of non-dimensional instantaneous streamwise velocity fluctuations u'/U_b in the x-z plane at the rib height ($y/\delta = 0.2$). Panels (a)-(c) correspond to cases P1, P2 and P3, respectively.

for discretization in the streamwise and vertical directions. In each finite element, a 4th-order Gauss-Lobatto-Legendre Lagrange polynomial was used for further interpolation of flow variables. Case P1 has the finest grid resolution with $N_x \times N_y \times N_z = 1201 \times 161 \times 240$ nodes. The streamwise grid resolutions varies for $0.7 \leq \Delta_x^+ \leq 4.4$, and the maximum value of Δ_y^+ of the first grid off the walls is 0.20 in all tested cases. To satisfy the demanding requirement of DNS on grid resolutions, the ratio of the Kolmogorov scale over grid size is limited to $0.1 \leq \Delta/\eta \leq 3.43$, where $\Delta = \sqrt[3]{\Delta_x \Delta_y \Delta_z}$. Overall, the discrete solution to the governing equations based on the Semtex code is highly accurate and the DNS results are of a spectral accuracy.

For each simulated ribbed flow case, 600 instantaneous flow fields over 35 large-eddy turnover times (LETOTs, defined as $\delta/u_{\tau R}$) were used for collecting statistics once the flow became fully-developed and statistically stationary after a precursor simulation. Here, $u_{\tau R}$ denotes the average friction velocity over the bottom rib-roughened wall. The simulations were conducted using the GREX supercomputer of the University of Manitoba. For each test case, approximately 200,000 CPU hours were spent for solving the velocity field and for collecting the flow statistics.

RESULTS AND DISCUSSION

Figure 2 shows the streamlines of the mean velocity field superimposed with contours of non-dimensional TKE k/U_b^2. The characteristic mean flow vortices are marked with A, B and C, corresponding to the large circulation bubble behind the ribs (A) and the small secondary vortices located at the corners of the windward and leeward sides of a rib (B and C, respectively). From figure 2, it is evident that the mean flow pattern of case P3 is typical of a k-type rough-wall flow. For cases P1 and P2, the mean flow skims over the ribs, which is typical of a d-type rough-wall flow. As shown in figure 2, it is clear that due to the presence of ribs, a strong internal shear layer (ISL) is induced above the recirculation bubble A, leading to an intensive local production of TKE. For all three ribbed cases, the region with high level of TKE locates around the midspan between two adjacent ribs (i.e., at $x'/\delta = 0.5$, 0.7 and 0.95 for cases P1, P2 and P3, respectively).

To demonstrate the influences of the pitch-to-height ratio on the streaky structures, figure 3 displays the contours of non-dimensional instantaneous streamwise velocity fluctua-

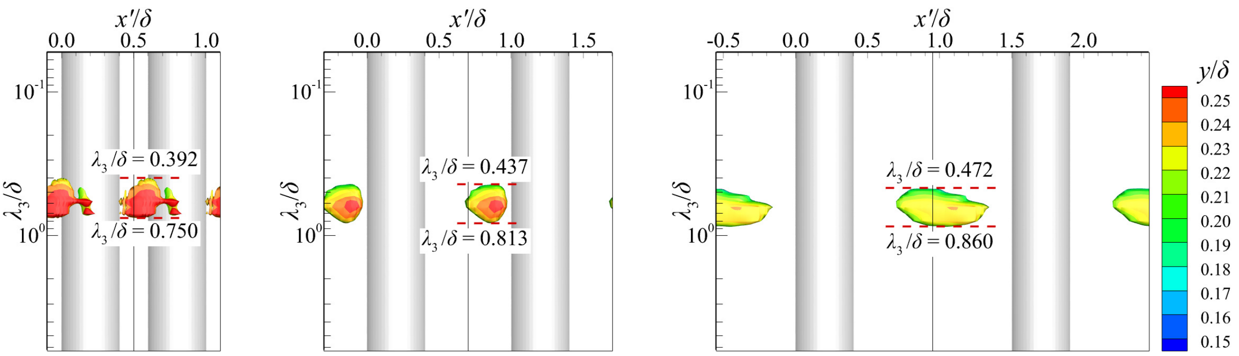

(a) case P1 (b) case P2 (c) case P3

Figure 4. Iso-surfaces of $k_3\Phi_k = 0.9\max(k_3\Phi_k)$ of the three ribbed cases. The red dashed lines demarcate the boundaries of the iso-surface.

tions u'/U_b in a x-z plane at the rib height $y/\delta = 0.2$. By comparing figures 3(a)-(c), it is observed that the strengths of the streaks enhances with an increasing value of P/H. As shown in figure 3(a), it is noted that a streaky structure can cover 2 or 3 rib periods along the streamwise direction in cases P1 and P2, resembling physical features typical of a d-type rough-wall flow. However, as the value of P/H increases to 7.5, energetic streaks in the ISL are broken up by the ribs in case P3, showing that the streaks are formed rather independently in each rib period, unaffected by the upstream flow. From figures 3(a)-(c), it is obvious that the spanwise spacing between high- and low-speed streaks increases as the value of P/H increases, showing a larger spanwise scale of turbulent motions.

To develop a deep insight into the characteristics spanwise scale of turbulence structures under the influence of pitch-to-height ratio, the energetic cores of the premultiplied spectrum $k_3\Phi_k$ of the three ribbed cases are demonstrated in figure 4 using the iso-surfaces of $k_3\Phi_k = 0.9\max(k_3\Phi_k)$, where $\Phi_k = \mathrm{Re}\{\overline{\widehat{u'_i}^*\widehat{u'_i}}\}/2$ is the spanwise energy spectra of TKE. Here, an overline $\overline{(\cdot)}$ denotes averaging over time t, and over all rib periods, and a hat $\widehat{(\cdot)}$ denotes the Fourier transform of an arbitrary variable. As shown in figure 4, it is observed that the most energetic region of the turbulence structures arises in the ISL around the midspan between two adjacent ribs, which is similar to the distribution of TKE in the physical space shown in figure 2. The iso-surface elongates along the streamwise direction as the value of P/H increases, and its vertical position centers around $H \pm 0.05\delta$, which sightly moves downwards to the ribbed wall with an increasing value of P/H. It is observed that as the value of P/H increases, the energetic flow structures expand spanwise such that the spanwise wavelengths corresponding to both upper and lower boundaries of the energetic core of flow structures increase. Moreover, from figure 4, it is observed that the size of the energetic core of turbulence structures increases from $\Delta\lambda_3/\delta = 0.324$ to 0.376 and 0.388 as the value of P/H increases from 3.0 to 5.0 and 7.5.

The transport equation of Reynolds stresses in the spectral space reads

$$\frac{\partial \overline{\widehat{u'_i}^*\widehat{u'_j}}}{\partial t} = -\widetilde{H}_{ij} + \widetilde{P}_{ij} + \widetilde{T}^s_{ij} + \widetilde{T}^p_{ij} + \widetilde{G}_{ij} + \widetilde{D}_{ij} + \widetilde{\Pi}_{ij} + \widetilde{\varepsilon}_{ij} = 0 \quad , \tag{1}$$

where $\widetilde{H}_{ij}$, $\widetilde{P}_{ij}$, Π_{ij}, $\widetilde{T}^s_{ij}$, $\widetilde{T}^p_{ij}$, $\widetilde{G}_{ij}$, $\widetilde{D}_{ij}$, $\widetilde{\Pi}_{ij}$ and $\widetilde{\varepsilon}_{ij}$ denote the convection, production, interscale transport, turbulence-diffusion, pressure-diffusion, viscous-diffusion, pressure-strain and dissipation terms. The definitions of these terms are given as

$$\widetilde{H}_{ij} = \mathrm{Re}\left\{ \langle u_1 \rangle \frac{\partial \overline{\widehat{u'_i}^*\widehat{u'_j}}}{\partial x_1} + \langle u_2 \rangle \frac{\partial \overline{\widehat{u'_i}^*\widehat{u'_j}}}{\partial x_2} \right\} \quad , \tag{2}$$

$$\widetilde{P}_{ij} = \mathrm{Re}\left\{ -\overline{\widehat{u'_k}^*\widehat{u'_j}}\frac{\partial\langle u_i\rangle}{\partial x_k} - \overline{\widehat{u'_k}\widehat{u'_i}^*}\frac{\partial\langle u_j\rangle}{\partial x_k} \right\} \quad , \tag{3}$$

$$\begin{aligned}\widetilde{T}^s_{ij} = \mathrm{Re}\Bigg\{ & -\overline{\widehat{u'_j}\frac{\partial \widehat{u'_iu'_1}^*}{\partial x_1}} - \overline{\widehat{u'_i}^*\frac{\partial \widehat{u'_ju'_1}}{\partial x_1}} - \overline{\widehat{u'_j}\frac{\partial \widehat{u'_iu'_2}^*}{\partial x_2}} - \overline{\widehat{u'_i}^*\frac{\partial \widehat{u'_ju'_2}}{\partial x_2}} \\ & + \frac{1}{2}\left(\frac{\partial \overline{\widehat{u'_iu'_1}^*\widehat{u'_j}}}{\partial x_1} + \frac{\partial \overline{\widehat{u'_iu'_2}^*\widehat{u'_j}}}{\partial x_2} + \frac{\partial \overline{\widehat{u'_ju'_1}\widehat{u'_i}^*}}{\partial x_1} + \frac{\partial \overline{\widehat{u'_ju'_2}\widehat{u'_i}^*}}{\partial x_2} \right) \\ & - \mathrm{i}k_3\left(\overline{\widehat{u'_i}^*\widehat{u'_ju'_3}} - \overline{\widehat{u'_j}^*\widehat{u'_iu'_3}} \right) \Bigg\} \quad ,\end{aligned} \tag{4}$$

$$\widetilde{T}^p_{ij} = \mathrm{Re}\left\{ -\frac{1}{2}\left(\frac{\partial \overline{\widehat{u'_iu'_1}^*\widehat{u'_j}}}{\partial x_1} + \frac{\partial \overline{\widehat{u'_iu'_2}^*\widehat{u'_j}}}{\partial x_2} + \frac{\partial \overline{\widehat{u'_ju'_1}\widehat{u'_i}^*}}{\partial x_1} + \frac{\partial \overline{\widehat{u'_ju'_2}\widehat{u'_i}^*}}{\partial x_2} \right) \right\} \quad , \tag{5}$$

$$\widetilde{G}_{ij} = \mathrm{Re}\left\{ -\frac{1}{\rho}\left(\frac{\partial \overline{\hat{p}'^*\hat{u}'_j}}{\partial x_1}\delta_{i1} + \frac{\partial \overline{\hat{p}'^*\hat{u}'_j}}{\partial x_2}\delta_{i2} + \frac{\partial \overline{\hat{p}'\hat{u}'^*_i}}{\partial x_1}\delta_{j1} + \frac{\partial \overline{\hat{p}'\hat{u}'^*_i}}{\partial x_2}\delta_{j2} \right) \right\} \quad , \tag{6}$$

$$\widetilde{D}_{ij} = \mathrm{Re}\left\{ \nu\left(\frac{\partial^2 \overline{\widehat{u'_i}^*\widehat{u'_j}}}{\partial x_1^2} + \frac{\partial^2 \overline{\widehat{u'_i}^*\widehat{u'_j}}}{\partial x_2^2} \right) \right\} \quad , \tag{7}$$

$$\begin{aligned}\widetilde{\Pi}_{ij} = \mathrm{Re}\Bigg\{ & \frac{1}{\rho}\Bigg(\overline{\widehat{p'}^*\frac{\partial \widehat{u'_j}}{\partial x_1}}\delta_{i1} + \overline{\widehat{p'}^*\frac{\partial \widehat{u'_j}}{\partial x_2}}\delta_{i2} + \overline{\widehat{p'}\frac{\partial \widehat{u'_i}^*}{\partial x_1}}\delta_{j1} + \overline{\widehat{p'}\frac{\partial \widehat{u'_i}^*}{\partial x_2}}\delta_{j2} \\ & + \mathrm{i}k_3\left(\overline{\widehat{p'}^*\widehat{u'_j}}\delta_{i3} - \overline{\widehat{p'}\widehat{u'_i}^*}\delta_{j3} \right) \Bigg) \Bigg\} \quad ,\end{aligned} \tag{8}$$

$$\widetilde{\varepsilon}_{ij} = \mathrm{Re}\left\{ -2\nu\overline{\frac{\partial \widehat{u'_i}^*}{\partial x_1}\frac{\partial \widehat{u'_j}}{\partial x_1}} - 2\nu\overline{\frac{\partial \widehat{u'_i}^*}{\partial x_2}\frac{\partial \widehat{u'_j}}{\partial x_2}} - 2\nu k_3^2\overline{\widehat{u'_i}^*\widehat{u'_j}} \right\} \quad . \tag{9}$$

The spectral budget terms of TKE can be obtained directly from the contraction of those of Reynolds stresses.

Figure 5 shows the profiles of the premultiplied budget terms in the spectral transport equation of TKE midway between two adjacent ribs at the vertical position corresponding to the peak of $k_3\Phi_k$ (i.e., at $[x'/\delta, y/\delta]$=[0.5, 0.238], [0.7, 0.203] and [0.95, 0.186] for cases P1, P2 and P3, respectively). From figure 5, it is obvious that the production term $\widetilde{P}_k$ is the dominant source term, and the turbulence-diffusion term $\widetilde{T}^p_k$, dissipation term $\widetilde{\varepsilon}_k$ and pressure-diffusion term $\widetilde{G}_k$ are the lead sink terms of TKE in the spectral space. From the profiles of $k_3\widetilde{T}^s_k$, it is evident that both forward and inverse energy transfers occur concurrently in a ribbed channel flow. Generally, TKE is transported from the energetic turbulent motions of moderate spanwise wavelength of approximately $\lambda_3/\delta = 0.5$ to the smaller- and larger-scale turbulence of $\lambda_3/\delta < 0.2$ and $\lambda_3/\delta > 2$ (corresponding to forward the backward scatters of TKE, respectively). However, overall, the forward scatter dominates the interscale transport of TKE. By a careful perusal of figure 5, it is observed that these budget terms differ in their characteristic spanwise wavelengths, indicating that the turbulence structures associated with the energy transport processes feature multiple spanwise scales. For instance, for the small wavelength of $\lambda_3/\delta < 0.2$ at which the forward energy

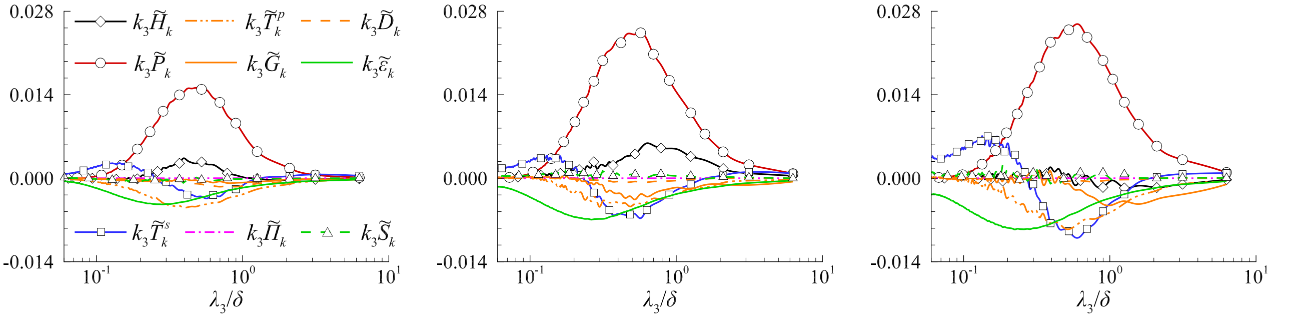

(a) case P1 (b) case P2 (c) case P3

Figure 5. Premultiplied budget terms in the spectral transport equation of TKE in the ribbed flows midway between two adjacent ribs. Panels (a)-(c) correspond to cases P1, P2 and P3 at $[x'/\delta, y/\delta] = [0.5, 0.238]$, [0.7, 0.203] and [0.95, 0.186], respectively. All the terms are non-dimensionalized by U_b^3/δ^2.

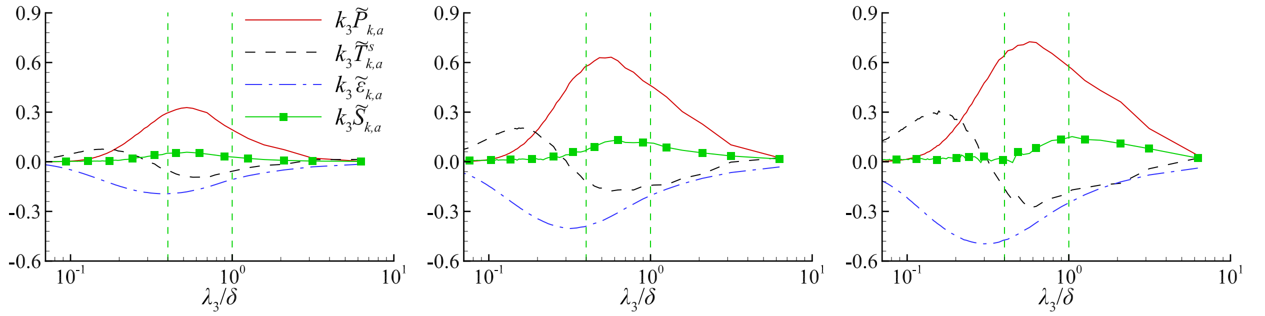

(a) case P1 (b) case P2 (c) case P3

Figure 6. Premultiplied vertical-averaged production, interscale transport, dissipation terms and the sum of these three terms midway between two adjacent ribs. All the terms are non-dimensionalized by $\max(k_3\widetilde{P}_k)_{sc}$. The green vertical dashed lines demarcate $\lambda_3/\delta = 0.4$ and 1.

scatter takes place, the budget balance of TKE is dominated by the interscale transport term $\widetilde{T}_k^s$ as the source and by the dissipation term $\widetilde{\varepsilon}_k$ as the sink. Around the moderate wavelength of $\lambda_3/\delta = 0.5$, $k_3\widetilde{T}_k^s$ is negatively-valued and becomes a significant sink of TKE. Meanwhile, $k_3\widetilde{P}_k$ and $k_3\widetilde{T}_k^p$ reach their maximum and minimum around $\lambda_3/\delta = 0.5$, becoming the lead source and sink of TKE, respectively. Moreover, by comparing figures 5(a)-(c), it is evident that the energy transport processes also differ in both magnitude and characteristic spanwise wavelengths among the three ribbed cases (P1-P3). For instance, it is clear that except for the convection term, all the other terms enhance as the value of P/H increases, corresponding to augmented TKE levels. Compared with $k_3\widetilde{T}_k^p$, the magnitude of $k_3\widetilde{T}_k^s$ enhances and gradually dominates the sink of TKE around $\lambda_3/\delta = 0.5$ as the value of P/H increases.

To compare the budget terms among the smooth and ribbed channel flow cases, all the premultiplied budget terms are non-dimensionalized by the maximum premultiplied production term of the smooth channel flow $\max(k_3\widetilde{P}_k)_{sc}$ hereinafter, denoted by a subscript '*non*', i.e., $(\cdot)_{non} = (\cdot)/\max(k_3\widetilde{P}_k)_{sc}$. In addition, based on the characteristic spanwise wavelengths shown in figure 5, the turbulence scales are separated and categorized as the "small" (for $0 < \lambda_3/\delta \leq 0.4$), "moderate" (for $0.4 < \lambda_3/\delta \leq 1$) and "large" (for $\lambda_3/\delta > 1$) scales for the purpose of comparison.

To further reveal the energy cascades between the production and dissipation of TKE in ribbed channel flows, figure 6 shows the vertical profiles of the premultiplied vertical-averaged production $k_3\widetilde{P}_{k,a}$, interscale transport $k_3\widetilde{T}_{k,a}^s$, dissipation $k_3\widetilde{\varepsilon}_{k,a}$ and the sum of these three terms $k_3\widetilde{S}_{k,a}$ at the midspan between two adjacent ribs, where $\widetilde{P}_{k,a} = \frac{1}{L_y}\int_0^{L_y}\widetilde{P}_k \mathrm{d}y$, $\widetilde{T}_{k,a}^s = \frac{1}{L_y}\int_0^{L_y}\widetilde{T}_k^s \mathrm{d}y$ and $\widetilde{\varepsilon}_{k,a} = \frac{1}{L_y}\int_0^{L_y}\widetilde{\varepsilon}_k \mathrm{d}y$. From figure 6, the difference in the characteristic wavelength between the production and dissipation terms is evident, and it is understood that it is the interscale transport term that harvests energy from the moderate- and large-scale turbulent motions to empower small-scale motions. It is noteworthy that the sum of these three terms is scanty for small-scale turbulences, i.e., $\widetilde{P}_{k,a} + \widetilde{T}_{k,a}^s + \widetilde{\varepsilon}_{k,a} \approx 0$ for $\lambda_3/\delta < 0.4$, showing that the total turbulent production at the midspan between two adjacent ribs is approximately balanced by the interscale transport and dissipation terms for small-scale turbulent motions. Figure 6 also indicates that the spatial transport of TKE along the streamwise direction features moderate and large scales, as indicated by the non-trivial values of $\widetilde{S}_{k,a}$ in such wavelength range.

Figure 7 compares the iso-surfaces of the non-dimensional premultiplied production term $(k_3\widetilde{P}_k)_{non}$ of the three ribbed cases. From the iso-surfaces, it is interesting to observe that the regions with very high level of TKE generation of $(k_3\widetilde{P}_k)_{non} > 5$ arises at $x'/\delta \approx 0.05$ and $x'/\delta \approx 0.25$ among the three ribbed cases, corresponding to the reattachment and detachment regions of the mean flow, respectively. Hence, isopleths of $(k_3\widetilde{P}_k)_{non}$ at these two special streamwise positions as well as the midspan between two adjacent ribs ($x'/\delta = 0.5$, 0.7 and 0.95 for cases P1, P2 and P3, respectively) are plotted in cross-stream planes A, B and C in figure 7. To highlight the rib enhancement on the turbulence production, regions of $(k_3\widetilde{P}_k)_{non} > 1$ are recognized as the enhanced production region where the production rate of TKE is larger than that of the smooth channel flow. As clearly shown in figure 7, the high production region arises in a large range in both x_1 and λ_3 directions in the ISL around $y/\delta = 0.2$, indicating that the production of TKE is highly

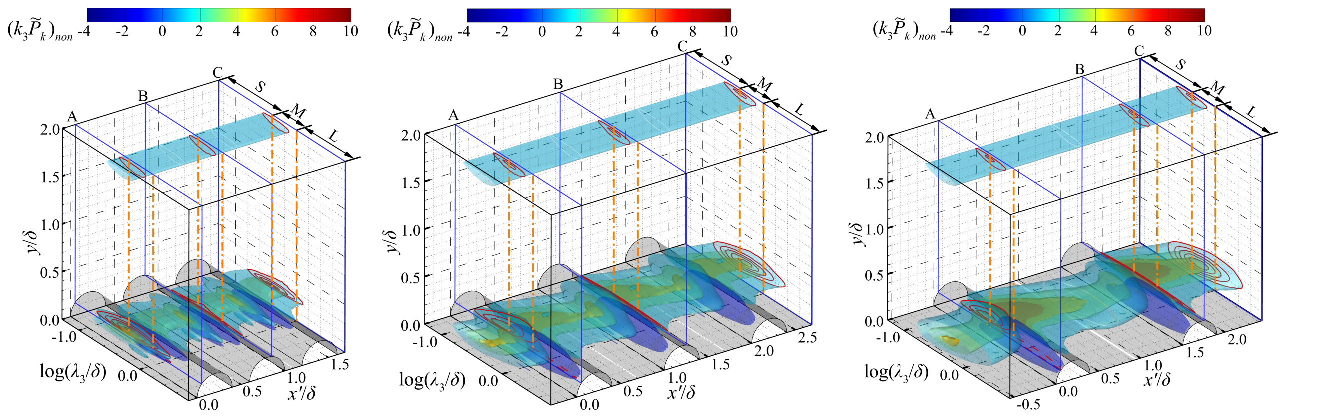

(a) case P1 (b) case P2 (c) case P3

Figure 7. Iso-surfaces of the premultiplied production term of the three ribbed cases. Isopleths of $(k_3\widetilde{P}_k)_{non}$ are shown in cross-stream (y-λ_3) planes located at relative streamwise positions $x'/\delta = 0.05$, 0.25 and at the midspan between two adjacent ribs (labelled as A, B and C, respectively). In vertical planes A, B and C, the outermost isopleth corresponds to $(k_3\widetilde{P}_k)_{non} = 1$, and the increment between two adjacent isopleths is 1. The vertical orange dashed-dotted lines demarcate spanwise non-dimensional wavelengths of $\lambda_3/\delta = 0.4$ and 1, and 'S', 'M' and 'L' denote small, moderate and large scales, respectively.

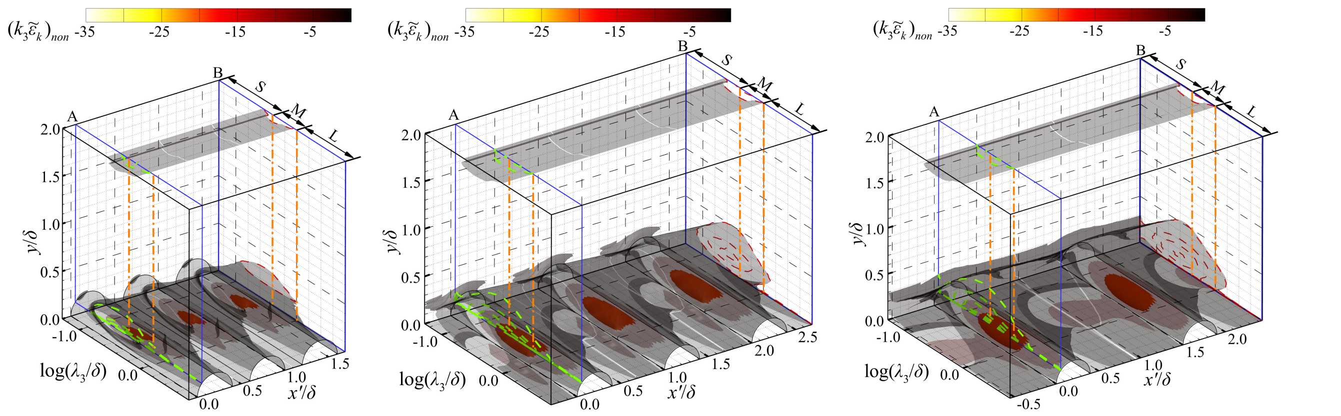

(a) case P1 (b) case P2 (c) case P3

Figure 8. Iso-surfaces of the premultiplied dissipation term of the three ribbed cases. Isopleths of $(k_3\widetilde{\varepsilon}_k)_{non}$ are shown in cross-stream (y-λ_3) planes located at relative streamwise positions $x'/\delta = 0.05$ and at the midspan between two adjacent ribs (labelled as A and B, respectively). In vertical planes A and B, the outermost isopleth corresponds to $(k_3\widetilde{\varepsilon}_k)_{non} = -0.5$, and the increment between two adjacent isopleths is -0.5. The vertical orange dashed-dotted lines demarcate spanwise non-dimensional wavelengths of $\lambda_3/\delta = 0.4$ and 1, and 'S', 'M' and 'L' denote small, moderate and large scales, respectively.

augmented near the ribbed bottom wall. As shown in figure 7, along the streamwise direction, the enhanced production region starts near the separation point around $x'/\delta = 0.25$, where a thin layer of high levels of $(k_3\widetilde{P}_k)_{non}$ develops in the streamwise direction, covering a relatively wide spanwise wavelength range of $\lambda_3/\delta \in [0.14, 2.10]$, $[0.12, 3.11]$ and $[0.11, 4.68]$ for cases P1, P2 and P3, respectively. As the shear layer develops along the streamwise direction, it is observed that the enhanced production region widens remarkably in the vertical direction, but narrows in the λ_3 direction immediately after the separation point. At the midspan between two adjacent ribs, the enhanced production region is mostly associated with the moderate scales around $\lambda_3/\delta = 0.5$ in all ribbed channel cases. Specifically, the spanwise wavelength ranges within $\lambda_3/\delta \in [0.16, 1.28]$, $[0.15, 2.30]$ and $[0.16, 2.99]$ for cases P1, P2 and P3, respectively, in the enhanced production region. Clearly, the TKE production for sustaining large-scale turbulent motions enhances gradually as the pitch-to-height ratio increases.

Figure 8 shows the iso-surfaces of the non-dimensional premultiplied dissipation term $(k_3\widetilde{\varepsilon}_k)_{non}$ of the three ribbed cases. It is observed that the dissipation of TKE is mainly attributed to the ribbed wall. The strongest dissipation takes place on the rib windward surface near the reattachment point around $x'/\delta = 0.05$ in all three ribbed channel cases, with $-(k_3\widetilde{\varepsilon}_k)_{non} > 20$. From the premultiplied spectrum $(k_3\widetilde{\varepsilon}_k)_{non}$ shown in figure 8, it is seen that this intensive wall dissipation is distributed among moderate scales for $0.4 < \lambda_3/\delta < 1$, and spreads to the ribbed bottom surfaces with decayed magnitudes. By comparing figures 8(a)-(c), it is obvious that the wall dissipation enhances in the inter-rib region as the pitch-to-height ratio increases.

Figure 9 displays the iso-surfaces of the non-dimensional premultiplied interscale transport term $(k_3\widetilde{T}_k^s)_{non}$ to further explain the energy cascade between turbulent motions of different scales in ribbed channel flows. As presented in figure 9, the energy transport from large- to small-scale turbulent motions is evident, consistent with the classical energy cascade process described by Richardson (Pope, 2000). At the midspan between two adjacent ribs, it is interesting to observe that in

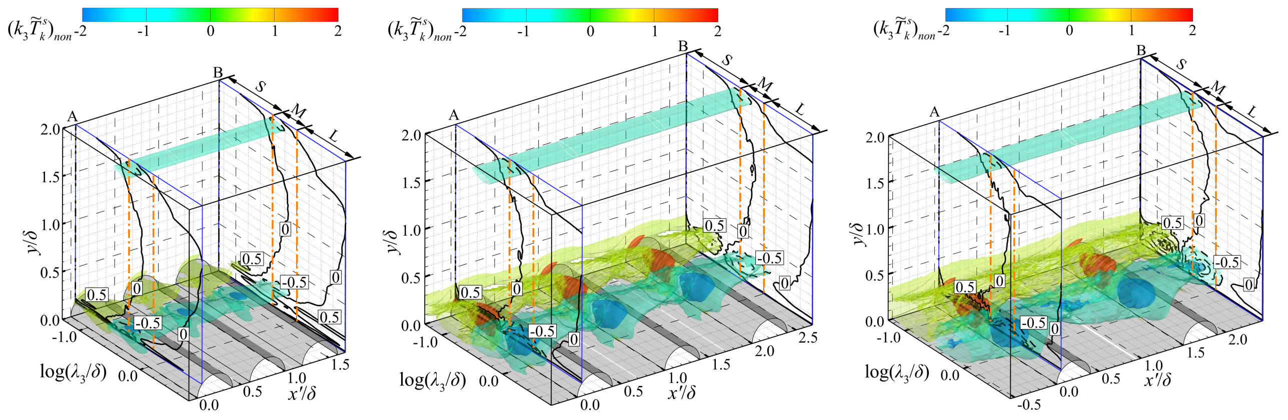

(a) case P1 (b) case P2 (c) case P3

Figure 9. Iso-surfaces of the premultiplied interscale transport term of the three ribbed cases. Isopleths of $(k_3\widetilde{T}_k^s)_{non}$ are shown in cross-stream (y-λ_3) planes located at $x'/\delta = 0.05$ and at the midspan between two adjacent ribs (labelled as A and B, respectively). In vertical planes A and B, the increment between two adjacent isopleths is 0.5. The vertical orange dashed-dotted lines demarcate spanwise non-dimensional wavelengths of $\lambda_3/\delta = 0.4$ and 1, and 'S', 'M' and 'L' denote small, moderate and large scales, respectively.

the ISL, the negatively-valued $k_3\widetilde{T}_k^s$ arises at moderate spanwise wavelengths around $\lambda_3/\delta \approx 0.5$, corresponding to the enhanced production region. In addition, the critical wavelength (corresponding to $k_3\widetilde{T}_k^s = 0$) associated with the forward energy transfer occurs at $\lambda_3/\delta \approx 0.2 \sim 0.3$ in the ISL near regions featuring high shear dissipation. It is understood that in the ISL, the interscale transport term absorbs energy associated with moderate scales from the production term, and then delivers it to small-scale turbulent motions to balance the dissipation. Moreover, it is seen that as the value of P/H increases, the strength of the interscale transport in the ISL enhances and the critical wavelength increases slightly as well. It is also observed that the flow impingement on the windward surface enhances the interscale transport of TKE dramatically, as the maximum and minimum of $k_3\widetilde{T}_k^s$ occur near the rib surface around $x'/\delta = 0.05$ in all ribbed channel cases. The interscale transport of TKE to the rib windward features similar spanwise wavelengths as those in the ISL, which increases with an increasing value of P/H. Furthermore, as shown in figure 9, the backscatter of TKE weakens as the value of P/H increases.

CONCLUSIONS

DNS of turbulent flows through a channel with circular-arc ribs mounted on one wall has been conducted to investigate the pitch-to-height ratio effects on the transport processes of TKE in the spectral space. In the physical space, it is observed that the region of high levels of TKE locates in the ISL induced by ribs. It is also observed that the spanwise spacing between high- and low-speed streaks increases as the value of P/H increases. By examining the premultiplied energy spectrum of TKE, it is confirmed that the spanwise characteristic scale of turbulent motions elongates as the value of P/H increases.

Through a comprehensive spectral analysis of the transport equation of TKE, it is observed that the total turbulent production at the midspan between two adjacent ribs is balanced approximately by the interscale transport and dissipation terms for small-scale motions (for $\lambda_3/\delta < 0.4$), while the spatial transport of TKE along the streamwise direction features moderate and large scales (for $\lambda_3/\delta > 0.4$). At the midspan between two adjacent ribs, the enhanced production region is mostly associated with the moderate scales around $\lambda_3/\delta = 0.5$ in all ribbed channel cases. With an increasing value of P/H, the TKE production for sustaining large-scale turbulent motions enhances. It is also observed that the dissipation of TKE peaks at the wall near the reattachment point around $x'/\delta = 0.05$, distributed among moderate scales of $0.4 < \lambda_3/\delta < 1$. Furthermore, it is interesting to observe that in the ISL at the midspan between two adjacent ribs, the negatively-valued $k_3\widetilde{T}_k^s$ arises at moderate spanwise wavelengths of approximately around $\lambda_3/\delta \approx 0.5$, and the critical wavelength corresponding to $k_3\widetilde{T}_k^s = 0$ occurs at $\lambda_3/\delta \approx 0.2 \sim 0.3$. It is worth noting that the backscatter of TKE weakens as the pitch-to-height ratio increases in the ribbed channel flows tested.

REFERENCES

Blackburn, H. M. & Sherwin, S. J. 2004 Formulation of a Galerkin spectral element–Fourier method for three-dimensional incompressible flows in cylindrical geometries. *J. Comp. Phys.* **197(2)**, 759–778.

Hoyas, S. & Jiménez, J. 2006 Scaling of the velocity fluctuations in the turbulent channels up to $Re_\tau = 2003$. *Phys. Fluids* **18**, 011702.

Kim, J., Moin, P., and Moser, R. (1987). Turbulence statistics in fully developed channel flow at low reynolds number. *J. Fluid. Mech.*, 177:133–166.

Lumley, J. L. 1964 Spectral energy budget in wall turbulence. *Phys. Fluids* **7**, 190–196.

Mansour, N. N., Kim, J. & Moin, P. 1988 Reynolds-stress and dissipation-rate budgets in a turbulent channel flow. *J. Fluid. Mech.* **194**, 15–44.

Mizuno, Y. 2016 Spectra of energy transport in turbulent channel flows for moderate Reynolds numbers. *J. Fluid. Mech.* **805**, 171–187.

Pope, S. B. (2000). *Turbulent Flows*. Cambridge University Press, 1st edition.

Prasad, B. N. & Saini, J. S. 1988 Effect of artificial roughness on heat transfer and friction factor in a solar air heater. *Sol. Energy* **46**, 555–560.

Yang, Z., Deng, B.-Q., Wang, B.-C. & Shen, L. 2020 Sustaining mechanism of Taylor–Görtler-like vortices in a streamwise-rotating channel flow. *Phys. Rev. Fluids* **5**, 044601.